Graphene Plasmon Reflection by Corrugations.

T. M. Slipchenko[1,*], M. L. Nesterov[2], R. Hillenbrand[3,4], A. Yu. Nikitin[3,5], and

L. Martín-Moreno[1,*]

[1] Instituto de Ciencia de Materiales de Aragón, CSIC, 50009 Zaragoza, Spain
[2] 4th Physics Institute and Research Center SCoPE, University of Stuttgart, Pfaffenwaldring 57, D-70550 Stuttgart, Germany
[3] IKERBASQUE Basque Foundation for Science, 48013 Bilbao, Spain.
[4] CIC nanoGUNE and UPV/EHU, Donostia-San Sebastián 20018, Spain
[5] CIC nanoGUNE, 20018 Donostia-San Sebastian, Spain

ABSTRACT: Graphene plasmons (GPs) exhibit extreme confinement of the associated electromagnetic fields. For that reason, they are promising candidates for controlling light in nanoscale devices. However, despite the ubiquitous presence of surface corrugations in graphene, very little is known on how they affect the propagation of GPs. Here we perform a comprehensive theoretical analysis of GP scattering by both smooth and sharp corrugations. For smooth corrugations, we demonstrate that scattering of GPs depends on the dielectric environment, being strongly suppressed when graphene is placed between two dielectrics with the same refractive indices. We also show that sharp corrugations can act as effective GP reflectors, even when their dimensions are small in comparison with the GP wavelength. Additionally, we provide simple analytical expressions for the reflectance of GP valid in an ample parametric range. Finally, we connect these results with potential experiments based on scattering scanning near-field optical microscopy (s-SNOM) showing how to extract the GP reflectance from s-SNOM images.

KEYWORDS: *graphene plasmon, graphene corrugations, plasmon scattering*

Graphene plasmons (GPs) - collective oscillations of free Dirac charge carriers in graphene coupled to electromagnetic fields - have an extremely short in-plane wavelength and are strongly confined to graphene sheet [1-5]. In addition, the GP wavelength depends on the Fermi level in graphene, and therefore can be manipulated by electrostatic gating. Lately, a great deal of attention has been devoted to the scattering characteristics of GPs by different inhomogeneities, as this is of particular importance for analyzing and controlling the GP propagation. GP efficient reflection has been already proved at graphene edges [6, 7], grain boundaries [8, 9], nanogaps in SiC terraces [10], boundaries introduced by ion beams [11], and at one-dimensional electrostatic barriers arising from a line of charges [12]. All previous cases can be related to conductivity inhomogeneities. Additionally, graphene also presents relief defects. In fact, free standing graphene is not flat. But neither it is graphene placed on a substrate (supported graphene), which has a tendency to form corrugations due to either imperfections of the substrate [13 - 15] or to the formation of graphene wrinkles (characterized by widths between one and tens of nm, heights below 15 nm and lengths above 100 nm) [16 - 21], ripples (which are corrugations with comparable height and width and smaller than wrinkles) [22] or bubbles (out-of-plane graphene deformations, with different shapes and sizes from tens to hundreds of nm in diameter and tens of nm in height, which accumulate air or other gas residuals between graphene and the substrate) [23 - 28].

The propagation of GPs can be strongly affected by the presence of these corrugations. However, very little is known about the scattering process, with the notable exception of ref. [28], which describes how a field hotspot can be formed by launching GPs in nano-bubbles.

2

In this paper, we theoretically study the GP scattering by corrugations in graphene. We focus on the effect of the change in spatial profile and assume that the conductivity is uniform along the defect. This is expected to be a good approximation for smooth corrugations [29, 30], while the realistic treatment of sharp corrugations would require a precise knowledge on how the graphene conductivity changes along the defect. In this last case, the results presented in this manuscript, together with those found for conductivity defects in flat graphene [9], can serve as a reference for a future theory on the scattering by a defect presenting both relief and conductivity changes.

We use both rigorous full-wave numeric simulations (see Methods) and an analytical approximation (valid for smooth corrugations), based in the Rayleigh expansion of the electromagnetic fields [31] and perturbation theory. Finally, we connect our theoretical analysis with potential scattering scanning near-field optical microscopy (s-SNOM) experiments. We simulate the near-field images that would be observed in s-SNOM experiments, and show how to extract the reflectance from them.

MODEL

We consider a one-dimensional relief defect in graphene, placed in the surface defined by $z = h(x)$. The region above graphene $(z > h(x))$ is filled by a superstrate characterized by a dielectric permittivity ε_1, while in the semi-infinite region $z < 0$ the permittivity is ε_3. The intermediate region $(h(x) > z > 0)$ is filled with a dielectric with permittivity ε_2. This configuration allows us to treat the scattering by both substrate corrugations (when $\varepsilon_2 = \varepsilon_3$, see Figure 1a), and by bubbles and

wrinkles (when $\varepsilon_2 \neq \varepsilon_3$, see Figure 3a). In this work we limit ourselves to single defects characterized by a Gaussian-shape corrugation [35]: $h(x) = h\exp[-4\,x^2/w^2]$, where w is the characteristic half-width and $h = h(0)$ is the corrugation height in its center ($x = 0$). We assume that the corrugation is shallow, i.e. $|h| \ll \lambda_p$. This profile provides a good approximation to realistic wrinkles on graphene arising for example in doped CVD grown graphene [20], or formed by the wedging transfer method [21]. We will analyze two differentiated main cases: (i) smooth defects, where $w \gg h$ (for which $|\partial_x h| \ll 1$) and (ii) sharp $w < h$ graphene corrugations.

Graphene is characterized by its conductivity $\sigma(\omega)$ (or the related adimensional conductivity $\alpha = 2\pi\,\sigma/c$, which we take from the random phase approximation (RPA) expressions [32-34]. As we are interested in defects that span a region smaller than the plasmon propagation length, we neglect absorption in graphene. Also, for definiteness, all results are presented assuming a Fermi energy $E_F = 0.2\,eV$, but this choice is not essential, as results only depend on E_F through the value of the GP wavevector.

In order to calculate the scattering coefficients, we consider a monocromatic GP (with frequency ω corresponding to a free-space wavelength λ, and plasmon wavelength λ_p) coming towards the defect from the region $x < 0$ and propagating along the $x-$ axis (see Figure 1a). After scattering, the GP can either reflect back, transmit to the region x > 0, or radiate out of the graphene surface.

However, in all considered cases, the out-of-plane scattering amplitude is orders of magnitude smaller than the reflection amplitude, due to the much larger density of plasmon modes than of radiation ones [9]. Thus, the GP scattering problem is characterized by providing either the transmission (t) or reflection (r) amplitudes. These quantities are linked, as energy flux conservation implies $T + R = 1$, where $T = |t|^2$ is the transmittance and $R = |r|^2$ is the reflectance.

RESULTS AND DISCUSSION

Smooth corrugations in graphene. Let us start by considering scattering by smooth substrate corrugations ($\varepsilon_2 = \varepsilon_3$). Figure 1b shows the numerically calculated reflectance spectra for corrugations in both symmetric ($\varepsilon_1 = \varepsilon_2 = \varepsilon_3 = 1$, green solid curve) and non-symmetric ($\varepsilon_1 = 1, \varepsilon_2 = \varepsilon_3 = 2.5$, red solid curve) dielectric environments. In both cases, the GP reflectance spectrum presents two spectral regions where scattering is negligible. For small wavelengths, the scattering regime is adiabatic (the GP "follows" the graphene profile), while for large GP wavelengths (larger than the defect dimensions) the scattering enters the "Rayleigh" regime [9, 31, 35-37]. In between these two limiting regimes, when $\lambda_p \sim w$, the plasmon neither follows adiabatically the corrugation not it encounters a defect of comparatively negligible size, and the reflectance presents a maximum.

Remarkably, the reflectance maximum strongly depends on whether the environment is symmetric or not. There are two apparent differences. First, $R(\lambda)$ peaks at a different wavelength: $\lambda = 8.8 \, \mu m$ for symmetric surrounding and $\lambda = 15.4 \, \mu m$ non-symmetric surrounding, respectively. This can be readily explained by the

dependence of the GP wavelength dielectric environment: $\lambda_p \approx 2\lambda \, \text{Im}(\alpha)/(\varepsilon_1 + \varepsilon_2)$.

Second, the GP reflectance by the corrugation is 2 orders of magnitude smaller in the symmetric environment than in the non-symmetric one. This change can be understood by noticing that, in the left panels of Figure 1a, a rotation of 180^0 around an axis perpendicular to the page transforms the corrugation $h(x)$ into $-h(x)$ and, simultaneously, transforms incidence from the left into incidence from the right. In a symmetric environment, the scatterer remains the same (the rotation being equivalent to looking at the scatterer from $z < 0$, instead of doing it from $z > 0$). As the system presents time reversal symmetry, the reflection amplitude is the same for left- and right- incidence. Thus, in a symmetric environment $r(h) = r(-h)$, implying that the Taylor series of r contains only even order terms. Thus, for small defects, $r \sim h^2$. In contrast, in the asymmetric environment an 180^0-rotated protrusion ($h(x) > 0$) would transform into a dielectric-filled indentation, which is different from the corrugation defined by $-h(x)$, which would be an air-filled indentation (see bottom left scheme in Figure 1a). Thus, in this case the two scattering geometries are not related and, in general, $r(h) \neq r(-h)$. This means that the Taylor expansion of r contains a linear term $r \sim h$. Since for small h the GP reflection amplitude is determined by the first term in its Taylor expansion in h, our general symmetry considerations can explain the significantly smaller GP reflection from the corrugation in the symmetric surrounding compared to that one in the non-symmetric surrounding. Note that such a dramatic difference in the GP reflectance between symmetric and non-symmetric dielectric environments does not occur for conductivity defects in flat graphene [9].

Up to now, our results have been based on the full-wave numeric simulations and general fundamental physical considerations. However, for shallow $(|h| \ll \lambda_p)$ and smooth $(h \ll w)$ corrugations, analytical expressions for the reflectance can be obtained by a perturbation expansion of the electromagnetic fields, expressed within the Rayleigh approximation [31, 37].

We present all cumbersome derivations in the Methods and Supporting Information and give here the final result. The GP reflectance in the first-order Born approximation (FOBA) for a Gaussian-shape corrugation reads simply as:

$$R_{FOBA} = |r_{FOBA}|^2 = \frac{\pi}{4}\left(k_p w\right)^2 e^{-\left(k_p w\right)^2/2}\delta^2, \qquad (1)$$

where $k_p \approx 2\pi/\lambda_p$ is the GP wavevector and the δ factor is given by

$$\delta = 2\frac{\varepsilon_2 - \varepsilon_1}{\varepsilon_2 + \varepsilon_1}k_p h . \qquad (2)$$

Figure 1b illustrates the comparison of $R(\lambda)$ calculated within the FOBA (red dashed curve) and the one computed with the help of the full wave numerical simulations (red solid curve). The excellent agreement between FOBA and full wave simulations validates the simple analytical expression given by eq. (1), and allows the computation of the reflectance of GP from corrugations without the need to perform numerical calculations, that are usually time-consuming due to the large different between the free space wavelength and the dimensions of the corrugation. Equation (1) provides a number of valuable points. First, R_{FOBA} is proportional to $(\varepsilon_2 - \varepsilon_1)^2$, thus vanishing for a symmetric dielectric environment. This is in accordance with our previous discussion that, in the symmetric environment, the reflection amplitude is given by higher-order terms in the Born series (leading to higher orders in h).

Second, with the help of eq. (1), we can find the wavelength λ^{max} at which $R(\lambda)$ has a maximum. To do this, we use the graphene conductivity in the Drude approximation [32-34]: $\text{Im}(\alpha) \approx \lambda \, \alpha_0 E_F/\pi\hbar c$, (where $\alpha_0 = 1/137$ is a fine-structure constant) and substitute it to eq. (1). Then, taking the derivative of R_{FOBA} with respect to λ and equating it to zero, we find

$$\lambda^{max} = \pi \sqrt{\frac{\hbar c(\varepsilon_1 + \varepsilon_2)}{2\,\alpha_0 E_F}}\, w \,. \tag{3}$$

and a maximum value of the reflectance:

$$R_{FOBA}^{max} = R(\lambda^{max}) = \frac{16\pi}{e^2}\left(\frac{\varepsilon_2 - \varepsilon_1}{\varepsilon_2 + \varepsilon_1}\right)^2 \frac{h^2}{w^2}. \tag{4}$$

Equation (3) shows that the spectral position of the reflectance λ^{max} depends upon the dielectric permittivities of both superstrate and substrate, thus confirming our previous arguments regarding the shift of λ^{max} for the GP in the symmetric and non-symmetric surroundings (see red and blue curves in Figure 1b).

In Figure 2 we show the reflectance spectra for smooth corrugations within an ample range of geometric parameters. Figure 2a renders $R(\lambda)$ for corrugations of different height, h, and the same width, w; while Figure 2b shows $R(\lambda)$ for the corrugations of different w and the same h. In all cases, the reflectance presents a maximum, with a spectral position that is more sensitive to the change of w than to the change of h (in agreement with the FOBA result, which predicts a λ^{max} independent of h) and with a magnitude that is sensitive to the aspect ratio w/h. The spectral position of λ^{max} predicted by FOBA (eq. (3)) and the corresponding values R_{FOBA}^{max} are shown by the square symbols in Figures 2a and 2b, matching well the maxima in the $R(\lambda)$ calculated with the help of full wave simulations.

Equations (3) and (4) suggest a universal scaling R/δ^2 as a function of w/λ_p. Figure 2c confirms the validity of this scaling for small smooth defects. In this representation, the maximum in reflection occurs when $w/\lambda_p \approx 1/\sqrt{2}\pi$ (being independent of δ) and equals to $(R_{FOBA}/\delta^2)^{max} = \pi/2e \approx 0.58$.

Corrugations on supported graphene can be also formed due to the buckling of the graphene sheet [23, 24]. Then, air (or other gases) can accumulate between the graphene corrugation and the substrate. This buckle-induced corrugations form both nano-scale bubbles and wrinkles [23 – 27, 28]. Here we analyze the reflection of the GP by a wrinkle – a two-dimensional analog of bubble – with a dielectric substance (characterized by a dielectric permittivity, ε_2) accumulated between the graphene layer and the substrate (see schematics in the inset to Figure 3a).

Figure 3a shows the full wave numerical simulations for the reflectance spectra of GP impinging on a wrinkle (with dimensions that roughly correspond to those of the elongated bubble discussed in [23, 27, 28]), for different substances accumulated underneath. As expected from our previous analysis (see Figure 1 and Figure 2), in all cases the GP reflectance spectra present a maximum. This maximum blueshifts (from $\lambda = 21.6\,\mu m$ to $\lambda = 20.8\,\mu m$) with the decrease of ε_2 (from $\varepsilon_2 = \varepsilon_3 = 4.5$ to $\varepsilon_2 = \varepsilon_1 = 1$), as indicated by the discontinuous black line, which serves as an eye-guide. We explain the blueshift by the change of the local plasmon wavelength in the wrinkle region ($-w < x < w$) originated by the modification of the dielectric environment (notice that the similar change of λ_p in graphene nanobubbles has been reported in [28]). Indeed, when ε_2 decreases, the local GP wavelength in the wrinkle region increases as $\propto (\varepsilon_1 + \varepsilon_2)^{-1}$. From the point of view of the GP, the increase of

λ_p implies an effective decrease of the wrinkle size (in particular, the wrinkle width). This interpretation allows the qualitative understanding of the results in Figure 3a in terms of those in Figure 2b, where the decrease of the wrinkle width results in the blueshift of the GP reflection maximum. Monitoring the shift of the GP reflection maximum can potentially allow for sensing of the dielectric permittivity of the substance accumulated under graphene wrinkles, specially, if this substance presents resonances in the spectral region where the GP reflectance is not negligible.

Small sharp graphene corrugations. Let us now consider the GP reflection from small ($w < \lambda_p$) Gaussian-shaped corrugations with aspect ratio $w/h \lesssim 1$.

Figure 4a shows the GP reflectance (calculated with the full wave numerical simulations) as a function of the corrugation half-width, *w,* for several corrugation heights, h and a fixed $\lambda_p = 120 \; nm$. For this value of λ_p, the exponential decay of the GP in the direction perpendicular to the graphene layer is characterized by the confinement length of $L_z = \lambda_p/(2\pi) \approx 19 \; nm$. Thus, even nanometer size defects (as those studied in Fig. 4) should strongly modify the plasmon wavefield. In the case of smooth defects we have seen that this modification is largely adiabatic but, as shown in Figure 4a, abrupt defects present very different scattering properties. In the two considered cases where $h > L_z$, there is a corrugation shape where the GP reflectance nearly reaches unity, $R \approx 1$, thus showing that the corrugation can act as a perfect reflector. Additionally, the GP reflectance can also present an "anti-resonance", where the GP propagates without reflection, i.e. $R \approx 0$ (see the case $h = 50 \; nm, w = 16.4 \; nm$). Both the large dependence of the spectral position of the maximum of R with h (as compared to the case of smooth corrugations, where λ^{max}

is independent of h) and the presence of a reflectance anti-resonance indicates that the scattering of GP by abrupt corrugations is very different for that by smooth ones.

In order to get physical insight in the scattering process, in Figure 4b-4d we show the spatial distribution of $|E_z(x,z)|$ for the corrugations with $h = 50\,nm$ and widths labeled by points P1-P3 in Figure 4a.

In the case of a relatively wide corrugation $w > \lambda_p/2$ (point P1, where $w = 80\,nm$), $|E_z(x,z)|$ clearly shows interference fringes on the left of the corrugation (the incidence side), arising from a partial reflection of the GP ($R = 0.18$ according to Figure 4a). These fringes also appear for the case $w = 36\,nm$ (point P2 in Figure 4a) but, contrary to the previous case, the field in the transmission region is negligible, as corresponds to near unity reflectance. The fact that the field extends beyond the corrugation maxima points out to an interference effect between partial scattering events at both sides of the corrugation apex. Finally, Figure 4d renders $|E_z(x,z)|$ for reflection anti-resonance, ($w = 16.4\,nm$, point P3 in Figure 4a). Here the rapid modulation of the field inside the nano-defect indicates that the transmission occurs through GP tunneling.

A detailed analysis of the intriguing phenomena observed in the scattering of GP by sharp corrugations goes beyond the scope of this manuscript. Nevertheless, we speculate that the strong GP reflection caused by the sharp corrugations (as well as the qualitatively different shift of the reflectance maxima as compared to that of smooths corrugations) can be explained by the excitation of localized GP modes ("cavity" modes) of the corrugation. A concentration of the electric field on the apex

11

of the narrow corrugation (seen in Figure 4d) can serve as a supporting argument in our hypothesis, although the latter has to be carefully checked in future studies. Note that the existence of the localized GPs in isolated graphene deformations has been already reported for wedges and grooves [38], bumps [39] and nanobubbles [28]. Our results suggest that graphene-based metasurfaces based on engineered sharp substrate corrugations should present a strong interaction with GP and thus be interesting for the control of their excitation and propagation.

Prospects for potential near-field experiments. The reflection of GP by corrugations can be characterized experimentally, by means of near-field microscopy. Currently, s-SNOM is the only experimental tool able to visualize plasmons in graphene in real space [40, 41]. s-SNOM utilizes an atomic force microscopy (AFM) tip which is illuminated with an external infrared laser beam. The tip converts the incident radiation into a strongly confined near-field at the tip apex, providing the necessary momentum to launch plasmons in graphene. When the GPs are back-reflected at the corrugations, characteristic interference patterns are observed in the near-field images. Analyzing the near-field images, it is possible to extract GP reflectance. Such technique is known as GP interferometry [6, 10, 28].

We perform a simple numerical simulation of a potential s-SNOM experiment, using a point-dipole source (see Figure 5a). As has recently been shown [42], the vertical component of electric field below the dipole, E_z, can serve as a good qualitative approximation for the s-SNOM signal. Therefore, we calculate the field below the dipole, E_z, as a function of the dipole position (x, y) and simulate a near-field (NF) image, $|E_z(x, y)|$, [10, 42]. In this simulation, and in contrast to previous sub-sections,

we take into account the absorption in graphene by retaining the real part of the graphene conductivity.

An example of the NF image of a corrugation on graphene is shown in Figure 5b. In the NF image we observe several fringes (composed of the alternating NF minima and maxima) parallel to the corrugation indicating the interference of the GPs launched by the dipole and the GPs reflected by the corrugation. The distance between neighboring NF minima (or maxima) far from the corrugation equals approximately to half of the GP wavelength, $\lambda_p/2$. Due to the finite propagation length of the GP, the amplitude of the fringes decays along the graphene sheet in both directions across the corrugation. The cross-sections of the near-field images across the corrugation (the NF profiles) for different illumination wavelengths, λ, are shown in Figure 5c. As λ increases the fringes broaden and the spacing between them increases, as expected from the increase of λ_p with λ.

Previous analysis of the NF images reported for terrace steps [10] revealed the reflection of GPs and allowed extracting the GP reflectance. Here we treat our simulated images as a numerical experiment, and find out whether we can extract from them the value of the GP reflectance. The reflectance can be found by fitting the NF profiles in Figure 5c with the function corresponding to the field profile of a scattered GP (see Methods). The results of our analysis are shown in Figure 5d. An excellent agreement between R extracted from the simulated NF profiles (square symbols) and R calculated from the GP scattering problem (black solid curve) proves the possibility to quantitatively characterize GP reflection by graphene corrugations by means of s-SNOM imaging.

CONCLUSION

In our paper we have performed a comprehensive theoretical analysis of the GP reflection by both sharp and smooth corrugations in graphene. For shallow and smooth corrugations we have provided simple analytical results for the GP reflectance, demonstrating its universality and validity in an ample range of geometric parameters and dielectric environments. We have shown that the breaking of the environment symmetry leads to a significant increase of the GP reflectance, which is proportional to $R \sim (\varepsilon_2 - \varepsilon_1)^2$. We have found that a sharp corrugation can act as total GP reflector, even though both its width and height are smaller than the GP wavelength. Finally, we have performed the simulation of the potential s-SNOM experiment, showing that it is possible to extract the GP reflectance from the near-field images.
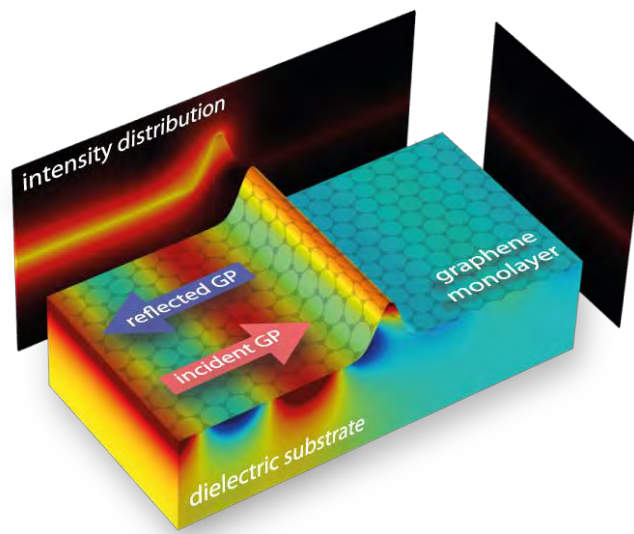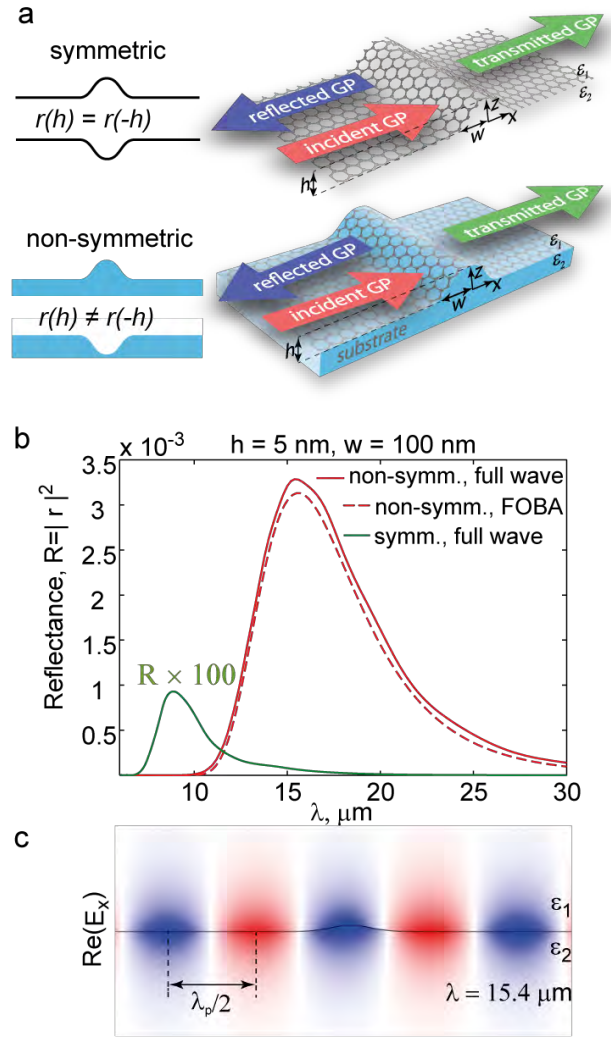
Figures

Figure TOC.

Figure 1: GP reflection from a graphene corrugation in symmetric and non-symmetric environment. (a) Schematics for GP scattering by corrugations, both for graphene on a substrate and for graphene in a symmetric dielectric environment. (b) Reflectance spectra $R(\lambda)$ for a GP impinging on a shallow Gaussian-shaped corrugation, for graphene on a substrate ($\varepsilon_1 = 1, \varepsilon_2 = 2.5$, red solid and dashed curves) and graphene in symmetric dielectric surrounding ($\varepsilon_1 = \varepsilon_2 = 1$, green solid curve). The corrugation width is $w = 100\,nm$ and the height is $h = 5\,nm$. (c) Snapshot of $\mathrm{Re}(E_x)$ for a GP propagating and impinging on the corrugation. The distance between maximum (red colored fringe) and minimum (blue colored fringe) of the electric field is equal to the half of the GP wavelength, $\lambda_p/2$.
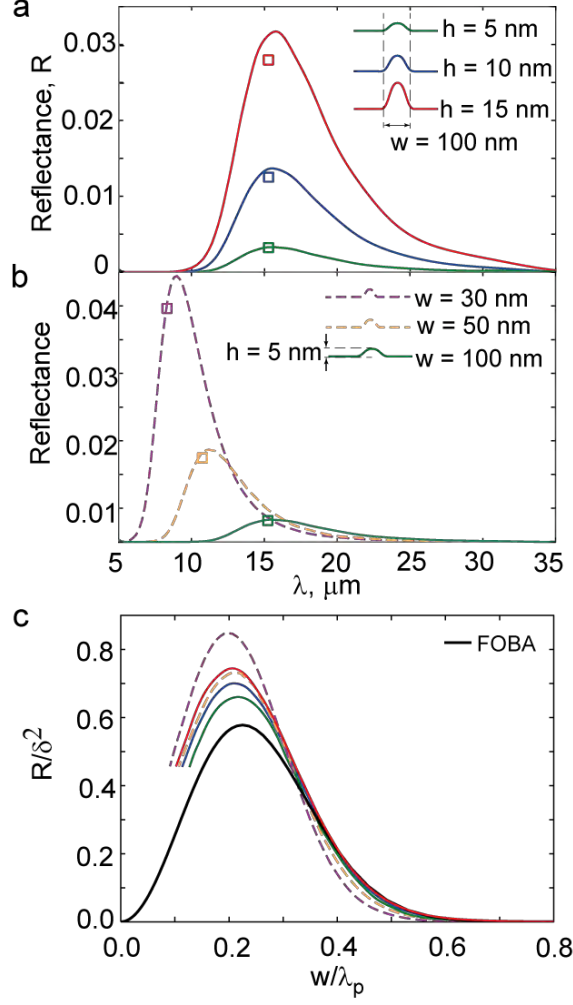
Figure 2: Reflectance spectra for a GP impinging on a Gaussian-shaped corrugation with different geometric parameters. (a) GP reflectance for corrugations of different heights and a fixed width $w = 100\ nm$ (b) GP reflectance for corrugations of different widths and a fixed height $h = 5\ nm$ (b). Square symbols in panels (a) and (b) correspond to $\lambda = \lambda^{max}$ and $R = R^{max}_{FOBA}$ calculated according to eqs. (3) and (4). (c) R/δ^2 as function of w/λ_p, for Gaussian-shaped corrugations with the same parameters as in the panels (a) and (b).
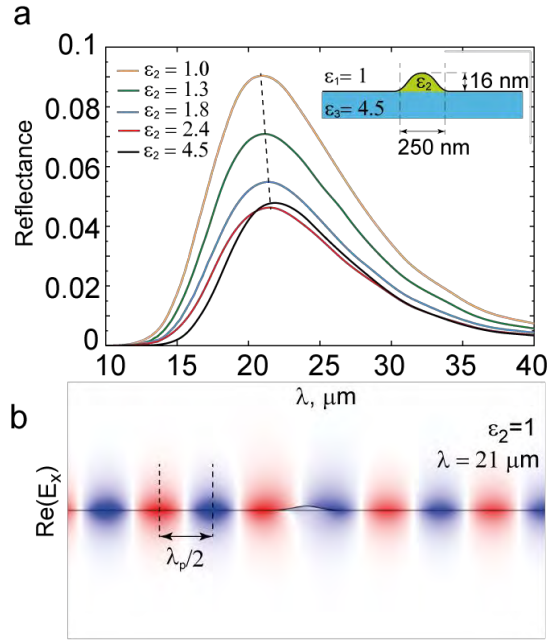
Figure 3: GP reflectance by a corrugation with different substances accumulated underneath. (a) Reflectance spectra for a GP impinging on a Gaussian-shaped corrugation with different ε_2 of the substances between graphene and substrate. The corrugation half-width is $w = 125\,nm$ and the height is $h = 16\,nm$. The discontinuous black line serves as an eye-guide to indicate the blueshift of the maximum. (b) Snapshot of $\text{Re}(E_x)$ for a GP impinging on the corrugation with $\varepsilon_2 = 1$.
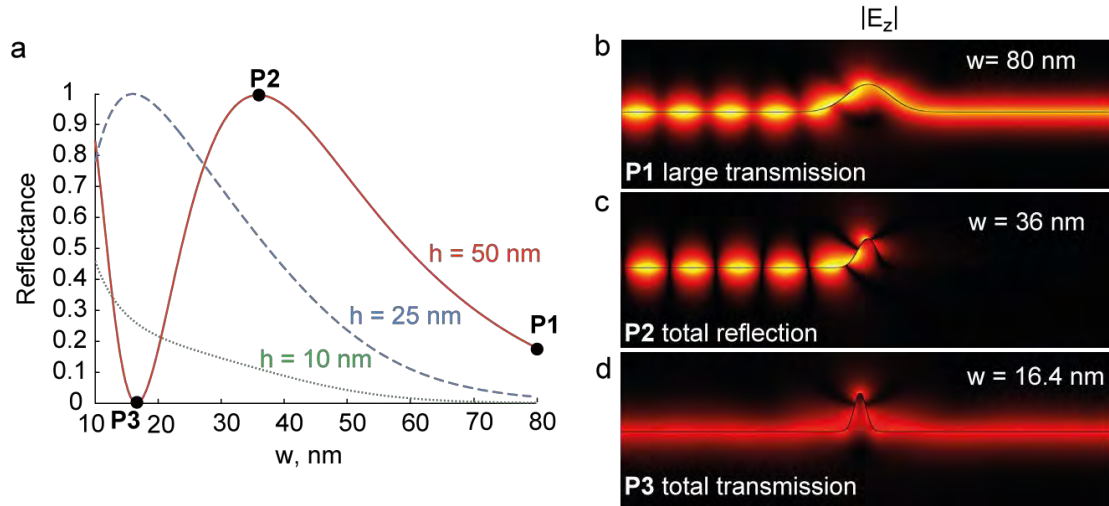
Figure 4: Reflectance of GPs from sharp corrugations. (a) Reflectance of a GP impinging on a sharp Gaussian-shaped corrugation as a function of corrugation half-width w, for different corrugation heights, h. The dielectric permittivity of the substrate is $\varepsilon_2 = 2.5$, and the considered free-space wavelength is $\lambda = 10\,\mu m$ ($\lambda_p = 0.12\,\mu m$). (b) - (d) Spatial distribution of $|E_z|$ corresponding to the points P1-P3 in (a).
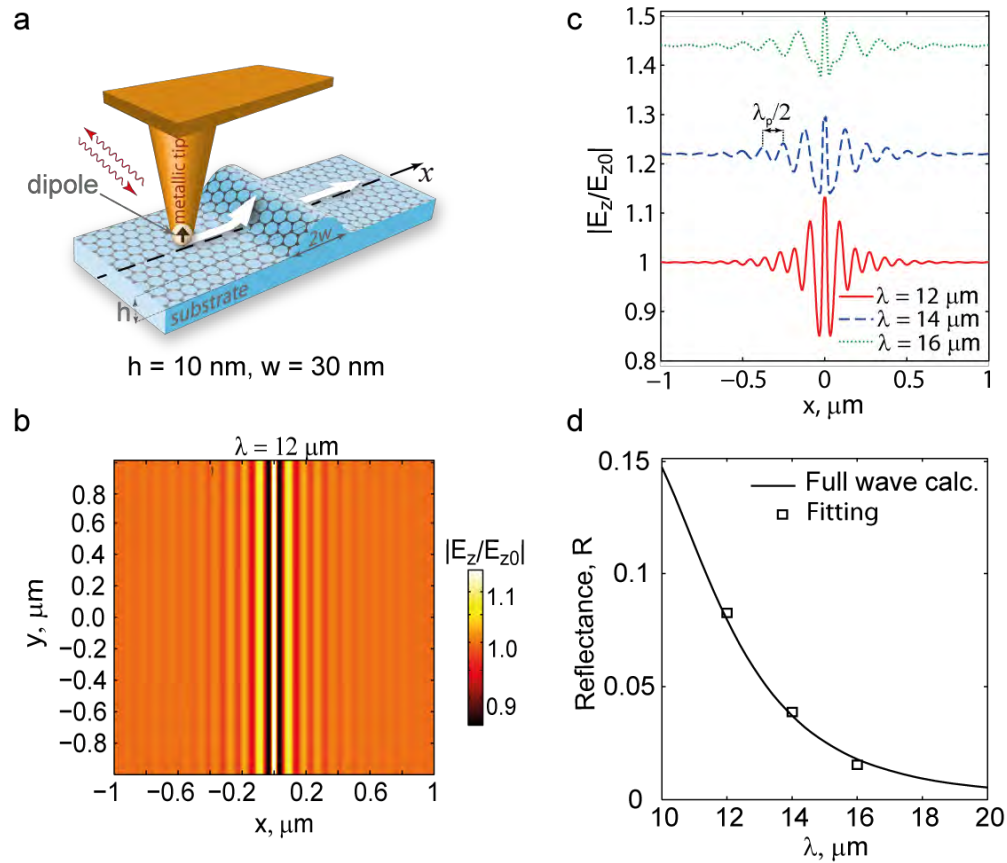
Figure 5: Simulation of an s-SNOM experiment. (a) Schematics of the simulation. We model the AFM tip by a simple electric dipole point-source. The dipole is located $80\ nm$ above graphene. (b) Simulated near-field image $|E_z(x,y)|$ at $\lambda = 12\ \mu m$. The field E_z is computed $10\ nm$ above graphene, below the dipole. (c) Line profile, $|E_z(x)|$, normalized to the value of the field far from the corrugation. (d) Wavelength spectrum of the GP reflectance calculated by the full wave simulation (solid curve) and extracted from the NF line profiles (square symbols). The relaxation time of the charge carriers in graphene is $\tau = 0.1\ ps$.

METHODS

Graphene parameters.

We do not take into account the losses in the graphene sheet for the computation of the GP reflectance, R, calculated numerically in Figures $1 - 4$. For the near-field simulations presented in Figure $5b, 5c$ we took the relaxation time of the charge carriers in graphene equal to $\tau = 0.1\ ps$. The good agreement between R extracted from the simulated near-field images and calculated numerically seen in Figure 5d justifies the neglect of losses in graphene in the scattering problem.

Perturbation theory. To treat the GP scattering problem analytically, we use the integral plane-wave expansion for the electromagnetic fields both in the superstrate (above graphene) and substrate (below graphene). We assume that all waves either propagate away, or decay from the graphene sheet (thus, no wave can propagate towards the sheet). Such approximate representation of the electromagnetic field is usually called Rayleigh expansion [31, 37]. Applying the boundary conditions for the electromagnetic fields at the graphene sheet and developing the series expansion of the resulting expressions in the small parameters $|h|/\lambda_p$ and $\partial_x h$ (up to the linear terms), we obtain a system of coupled integral equations for the scattered field amplitudes (see Supplementary information). These coupled integral equations must, in general, be solved numerically, by discretizing them in momentum space and appropriately truncating the resulting infinite discrete system of equations to guarantee the required precision. For smooth corrugations, the amplitude of the reflected GP can be analytically found from the solution of the coupled integral equations in the FOBA.

First principle numerical simulation. Full wave electromagnetic simulations were performed using the COMSOL software based on finite-element methods in frequency domain. The graphene layer was modelled as a surface current in the boundary conditions. In order to achieve convergence, the mesh element size in the vicinity of graphene was much smaller than both the plasmon wavelength and the corrugation height.

Simulation of the s-SNOM experiment. In the simulation, the tip was modelled by a vertical point dipole source (polarized along z-axis). We assume that the vertical component of the field below the dipole, E_z, approximates the signal scattered from the tip [42]. We simulated the near-field images (as the one shown in Figure 5b) by recording the calculated E_z as a function of the dipole position, x (due to the translational symmetry of the problem along the y-axis, E_z does not depend upon y).

Extraction of the GP reflectance from the near-field profiles. The electric field at a position between the dipole and the graphene sheet consists of both the NF generated by the dipole and the field of the reflected GP. We also take into account the GP excited due to the scattering of the dipole radiation by the corrugation and propagating in the same direction with the reflected GP. Thus, E_z can be approximated as

$$E_z = 1 + \frac{r}{1+C}\,e^{-i(2k_p x + \varphi)} + \frac{\eta}{1+C}\,e^{-i(k_p x + \phi)} \qquad \text{(M1)}$$

where r and φ are the GP reflection amplitude and phase, while η and ϕ are the amplitude and phase of the GP launched by the corrugation. With the help of the parameter $C \approx 1.53$ we take into account an average background signal

22

(corresponding to the non-plasmonic near field generated by the dipole over the sample). By fitting the simulated near-field profiles (shown in Figure 5c) with the help of equation (M1) we find the GP reflectance, $R = |r|^2$.

ASSOCIATED CONTENT

The manuscript has additional information and figures. This material is available free of charge via the Internet.

AUTHOR INFORMATION

Corresponding Authors

[*] Email: lmm@unizar.es

[*] Email: tetiana@unizar.es

Notes

The authors declare no competing financial interest.

ACKNOWLEDGMENTS

REFERENCES

1.   Novoselov, K. S.; Geim, A. K.; Morozov, S. V.; Jiang, D.; Zhang, Y.; Dubonos, S. V.; Grigorieva, I. V.; Firsov, A. A. Electric Field Effect in Atomically Thin Carbon Films. *Science* **2004**, 306 (5696), 666.
2.   Jablan, M.; Buljan, H.; Soljačić, M. Plasmonics in graphene at infrared frequencies. *Physical Review B* **2009**, 80 (24), 245435.
3.   Nikitin, A. Y.; Guinea, F.; Garcia-Vidal, F. J.; Martin-Moreno, L. Fields radiated by a nanoemitter in a graphene sheet. *Physical Review B* **2011**, 84 (19), 195446.
4.   Koppens, F. H. L.; Chang, D. E.; García de Abajo, F. J. Graphene Plasmonics: A Platform for Strong Light–Matter Interactions. *Nano Letters* **2011**, 11 (8), 3370-3377.
5.   Ju, L.; Geng, B.; Horng, J.; Girit, C.; Martin, M.; Hao, Z.; Bechtel, H. A.; Liang, X.; Zettl, A.; Shen, Y. R.; Wang, F. Graphene plasmonics for tunable terahertz metamaterials. *Nat Nano* **2011**, 6 (10), 630-634.
6.   Chen, J.; Badioli, M.; Alonso-Gonzalez, P.; Thongrattanasiri, S.; Huth, F.; Osmond, J.; Spasenovic, M.; Centeno, A.; Pesquera, A.; Godignon, P.; Zurutuza Elorza, A.; Camara, N.; de Abajo, F. J. G.; Hillenbrand, R.; Koppens, F. H. L. Optical nano-imaging of gate-tunable graphene plasmons. *Nature* **2012**, 487 (7405), 77-81.
7.   Fei, Z.; Rodin, A. S.; Andreev, G. O.; Bao, W.; McLeod, A. S.; Wagner, M.; Zhang, L. M.; Zhao, Z.; Thiemens, M.; Dominguez, G.; Fogler, M. M.; Neto, A. H. C.; Lau, C. N.; Keilmann, F.; Basov, D. N. Gate-tuning of graphene plasmons revealed by infrared nano-imaging. *Nature* **2012**, 487 (7405), 82-85.
8.   Fei, Z; Rodin, A. S.; GannettW; DaiS; ReganW; WagnerM; Liu, M. K.; McLeod, A. S.; DominguezG; ThiemensM; Castro NetoAntonio, H.; KeilmannF; ZettlA; HillenbrandR; Fogler, M. M.; Basov, D. N. Electronic and plasmonic phenomena at graphene grain boundaries. *Nat Nano* **2013**, 8 (11), 821-825.
9.   Garcia-Pomar, J. L.; Nikitin, A. Y.; Martin-Moreno, L. Scattering of Graphene Plasmons by Defects in the Graphene Sheet. *ACS Nano* **2013**, 7 (6), 4988-4994.
10.   Chen, J.; Nesterov, M. L.; Nikitin, A. Y.; Thongrattanasiri, S.; Alonso-González, P.; Slipchenko, T. M.; Speck, F.; Ostler, M.; Seyller, T.; Crassee, I.; Koppens, F. H. L.; Martin-Moreno, L.; García de Abajo, F. J.; Kuzmenko, A. B.; Hillenbrand, R. Strong Plasmon Reflection at Nanometer-Size Gaps in Monolayer Graphene on SiC. *Nano Letters* **2013**, 13 (12), 6210-6215.
11.   Weiwei, L.; Wei, C.; Wei, W.; Yinxiao, X.; Mengxin, R.; Xinzheng, Z.; Jingjun, X. Tailorable reflection of surface plasmons in defect engineered graphene. *2D Materials* **2016**, 3 (4), 045001.
12.   Torre, I.; Katsnelson, M., I.; Diaspro, A.; Pellegrini, V.; Polini, M. Lippmann-Schwinger theory for two-dimensional plasmon scattering [arXiv:1702.04925].
13.   Ishigami, M.; Chen, J. H.; Cullen, W. G.; Fuhrer, M. S.; Williams, E. D., *Atomic Structure of Graphene on SiO2*. **Nano Letters** 2007, 7 (6), 1643-1648.
14.   Geringer, V.; Liebmann, M.; Echtermeyer, T.; Runte, S.; Schmidt, M.; Rückamp, R.; Lemme, M. C.; Morgenstern, M., Intrinsic and extrinsic corrugation of monolayer graphene deposited on SiO_2. *Physical Review Letters* **2009**, 102 (7), 076102.
15.   Sinitskii, A.; Kosynkin, D. V.; Dimiev, A.; Tour, J. M., Corrugation of Chemically Converted Graphene Monolayers on SiO2. *ACS Nano* **2010**, 4 (6), 3095-3102.
16.   Li, X.; Cai, W.; An, J.; Kim, S.; Nah, J.; Yang, D.; Piner, R.; Velamakanni,

A.; Jung, I.; Tutuc, E.; Banerjee, S. K.; Colombo, L.; Ruoff, R. S. Large-Area Synthesis of High-Quality and Uniform Graphene Films on Copper Foils. *Science* **2009**, 324 (5932), 1312.

17.   Berger, C.; Song, Z.; Li, X.; Wu, X.; Brown, N.; Naud, C.; Mayou, D.; Li, T.; Hass, J.; Marchenkov, A. N.; Conrad, E. H.; First, P. N.; de Heer, W. A. Electronic Confinement and Coherence in Patterned Epitaxial Graphene. *Science* **2006**, 312 (5777), 1191.

18.   Schniepp, H. C.; Li, J.-L.; McAllister, M. J.; Sai, H.; Herrera-Alonso, M.; Adamson, D. H.; Prud'homme, R. K.; Car, R.; Saville, D. A.; Aksay, I. A. Functionalized Single Graphene Sheets Derived from Splitting Graphite Oxide. *The Journal of Physical Chemistry B* **2006**, 110 (17), 8535-8539.

19.   Xu, K.; Cao, P.; Heath, J. R. Scanning Tunneling Microscopy Characterization of the Electrical Properties of Wrinkles in Exfoliated Graphene Monolayers. *Nano Letters* **2009**, 9 (12), 4446-4451.

20.   Singh, A. K.; Iqbal, M. W.; Singh, V. K.; Iqbal, M. Z.; Lee, J. H.; Chun, S.-H.; Shin, K.; Eom, J. Molecular n-doping of chemical vapor deposition grown graphene. *Journal of Materials Chemistry* **2012**, 22 (30), 15168-15174.

21.   Calado, V. E.; Schneider, G. F.; Theulings, A. M. M. G.; Dekker, C.; Vandersypen L. M. K. Formation and control of wrinkles in graphene by the wedging transfer method. *Applied Physics Letters* **2012**, 101 (10), 103116.

22.   Deng, S.; Berry, V. Wrinkled, rippled and crumpled graphene: an overview of formation mechanism, electronic properties, and applications. *Materials Today* **2016**, *19* (4), 197-212.

23.   Pan, W.; Xiao, J.; Zhu, J.; Yu, C.; Zhang, G.; Ni, Z.; Watanabe, K.; Taniguchi, T.; Shi, Y.; Wang, X. Biaxial Compressive Strain Engineering in Graphene/Boron Nitride Heterostructures. *Scientific Reports* **2012**, 2, 893.

24.   Zhang, K.; Arroyo, M. Understanding and strain-engineering wrinkle networks in supported graphene through simulations. *Journal of the Mechanics and Physics of Solids* **2014**, 72, 61-74.

25.   Stolyarova, E.; Stolyarov, D.; Bolotin, K.; Ryu, S.; Liu, L.; Rim, K. T.; Klima, M.; Hybertsen, M.; Pogorelsky, I.; Pavlishin, I.; Kusche, K.; Hone, J.; Kim, P.; Stormer, H. L.; Yakimenko, V.; Flynn, G. Observation of Graphene Bubbles and Effective Mass Transport under Graphene Films. *Nano Letters* **2009**, 9 (1), 332-337.

26.   Georgiou, T.; Britnell, L.; Blake, P. ; Gorbachev, R.; Gholinia, A.; Geim, A. K. ; Casiraghi, C.; Novoselov, K. S. Graphene bubbles with controllable curvature. *Applied Physics Letters* **2011**, 99 (9), 093103.

27.   Khestanova, E.; Guinea, F.; Fumagalli, L.; Geim, A. K.; Grigorieva, I. V. Universal shape and pressure inside bubbles appearing in van der Waals heterostructures. *Nat. Commun.* **2016**, 7, 12587.

28.   Fei, Z.; Foley, J. J.; Gannett, W.; Liu, M. K.; Dai, S.; Ni, G. X.; Zettl, A.; Fogler, M. M.; Wiederrecht, G. P.; Gray, S. K.; Basov, D. N. Ultraconfined Plasmonic Hotspots Inside Graphene Nanobubbles. *Nano Letters* **2016**, 16 (12), 7842-7848.

29.   Eun-Ah, K.; Neto, A. H. C. Graphene as an electronic membrane. *EPL (Europhysics Letters)* **2008**, 84 (5), 57007.

30.   Deshpande, A.; Bao, W.; Miao, F.; Lau, C. N.; LeRoy, B. J. Spatially resolved spectroscopy of monolayer graphene on SiO_2. *Physical Review B* **2009**, 79 (20), 205411.

31.   Tsang, L., Kong, J. A., and Ding, K.-H.; *Scattering of Electromagnetic Waves: Theories and Applications*; Wiley:New York, 2000; pp 9-18.

32.   Wunsch, B.; Stauber, T.; Sols, F.; Guinea, F. Dynamical Polarization of Graphene at Finite Doping. *New J. Phys.* **2006**, 8, 318.

33.   Hwang, E. H.; Das Sarma, S. Dielectric Function, Screening, and Plasmons in Two-Dimensional Graphene. *Phys. Rev. B* **2007**, 75, 205418.

34.   Falkovsky, L. A. Optical Properties of Graphene and IV-VI Semiconductors. *Phys.-Usp.* **2008**, 51, 887.

35.   Nikitin, A. Y.; López-Tejeira, F.; Martín-Moreno, L. Scattering of Surface Plasmon Polaritons by One-Dimensional Inhomogeneities. *Phys. Rev. B* **2007**, 75, 035129.

36.   Sánchez-Gil, J. A.; Maradudin, A. A. Near-Field and Far-Field Scattering of Surface Plasmon Polaritons by One-Dimensional Surface Defects. *Phys. Rev. B* **1999**, 60, 8359–8367.

37.   Born, M., and Wolf, E.; *Principles of Optics;* Oxford:Pergamon, 1980; pp 647-656.

38.   Liu, P.; Zhang, X.; Ma, Z.; Cai, W.; Wang, L.; Xu, J. Surface plasmon modes in graphene wedge and groove waveguides. *Opt. Express* **2013**, 21 (26), 32432-32440.

39.   Smirnova, D.; Mousavi, S. H.; Wang, Z.; Kivshar, Y. S.; Khanikaev, A. B. Trapping and Guiding Surface Plasmons in Curved Graphene Landscapes. *ACS Photonics* **2016**, 3 (5), 875-880.

40.   Keilmann, F.; Hillenbrand, R. Near-field microscopy by elastic light scattering from a tip. *Philos. Trans. R. Soc. London*, Ser. A **2004**, 362, 787−805.

41.   Ocelic, N.; Huber, A.; Hillenbrand, R. Pseudoheterodyne detection for background-free near-field spectroscopy. *Appl. Phys. Lett.* **2006**, 89, 101124.

42.   Nikitin, A. Y.; Alonso González, P.; Vélez, S; Mastel, S; Centeno, A; Pesquera, A; Zurutuza, A; Casanova, F; Hueso, L. E.; Koppens, F. H. L.; Hillenbrand, R. Real-space mapping of tailored sheet and edge plasmons in graphene nanoresonators. *Nat Photon* **2016**, 10 (4), 239-243.